$$R = \sqrt[3]{\left(\frac{Eh}{2\pi(1-\sigma^3)}\right)\frac{\Delta V}{\Delta P}} \cdots (2)$$

where ΔV: change of pulsed wave volume, ΔP: change of pulsed wave pressure, R: radius of vessel, h: thckness of vessel wall, E: Young's elastic modulus, σ: Poisson's ratio, respectively. If the changes of R, h, E and σ before and after occlusion were considered very small, the relative change of radius of the vessel is expressed as equation. (3),

$$\%FMD = \frac{R_r - R_c}{R_c} \times 100$$

$$= \frac{\sqrt[3]{\left(\frac{Eh}{2\pi(1-\sigma^3)}\right)\frac{\Delta V_r}{\Delta P_r}} - \sqrt[3]{\left(\frac{Eh}{2\pi(1-\sigma^3)}\right)\frac{\Delta V_c}{\Delta P_c}}}{\sqrt[3]{\left(\frac{Eh}{2\pi(1-\sigma^3)}\right)\frac{\Delta V_c}{\Delta P_c}}} \times 100$$

$$= \left(\sqrt[3]{\frac{P_c \cdot V_r}{P_r \cdot V_c}} - 1\right) \times 100 \cdots (3)$$

where ΔV_c: change of pulsed wave volume at control, ΔP_c: change of pulsed wave pressure at control, R_c: radius of vessel at control, ΔV_r: change of pulsed wave volume after hyperemia, ΔP_r: change of pulsed wave pressure after hyperemia, R_r: radius of vessel after hyperemia, respectively.

Results

None of the subjects was injured nor felt sick in the experiment. Figure 2 shows a result of one of the volunteers (44 years old. male) showing the relation between %FMDus (relative FMD measured by ultrasound) and %FMDimp (relative FMD calculated by the proposed method).

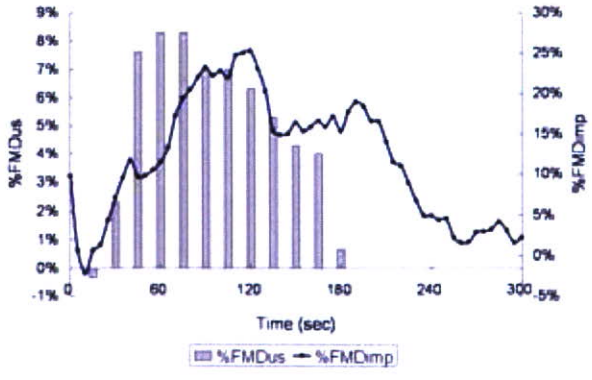

Figure 2: The Result of One of the Volunteers

Biphasic peaks at 120 and 190 sec were observed in %FMDimp while a single peak response was observed at 60 sec after occlusion in %FMDus. The peak was 25% in %FMDimp while it was 8% in %FMDus as reported as normal in the previous studies.

Discussion

Relative FMD (%FMDimp) was successfully obtained by the fully automatic measurement system proposed in the present study. Checking the calculated values beat by beat, the values were robust throughout the measurement. The discrepancy of %FMDimp from %FMDus may be explained that the blood volume of brachial artery alone was not measured by pulsed wave volume. The blood volume of whole vascular system in the forearm including arteries, capillaries, arterioles and veins, may be calculated by pulsed wave volume method. Originally, FMD was caused from the release of NO from occluded region where shear stress was strongly applied. In the sense whole vascular system was affected by NO release, %FMDimp may have its own important meanings in assessment of vascular endothelial function. Also, %FMDimp has a great advantage to conventional FMD measurement because it can be obtained fully automatically.

Conclusions

Relative FMD change (%FMDimp) was automatically measured by analyzing pulsed wave pressure and pulsed wave volume relationship. The result of the calculation was robust and %FMDimp was successfully obtained automatically. Although the peak time and percentage were different from those obtained by conventional ultrasound measurement, %FMDimp may have its own importance in the assessment of vascular endothelial function.

References

[1] FAULX MD, WRIGHT AT, HOIT B. (2003): 'Detection of endothelial dysfunction with brachial artery ultrasound scanning', *Am. Heart J.* **145**, pp. 943-51.

[2] BARTH JD. (2001): 'Which tools are in your cardiac workshop? Carotid ultrasound, endothelial function, and magnetic resonance imaging', *Am J Cardiol.* **87** pp. 8A-14A.

[3] KIMURA Y, MATSUMOTO M, DEN YB, IWAI K, MUNEHIRA J, HATTORI H, HOSHINO T, YAMADA K, KAWANISHI K, TSUCHIYA H. (1999): 'Impaired endothelial function in hypertensive elderly patients evaluated by high resolution ultrasonography', *Can J Cardiol.* **15** pp. 563-8.

[4] JODOIN I, BUSSIERES LM, TARDIF JC, JUNEAU M. (2001): 'Effect of a short-term primary prevention program on endothelium-dependent vasodilation in adults at risk for atherosclerosis', *Can J Cardiol.* **15** pp. 83-8.

Acoustic Impedance Micro-imaging for Biological Tissue Using a Focused Acoustic Pulse with a Frequency Range up to 100 MHz

N. Hozumi, A. Kimura, S. Terauchi, M. Nagao, S. Yoshida
Toyohashi University of Technology
Toyohashi, Japan
hozumi@eee.tut.ac.jp

K. Kobayashi
Honda Electronics Co., Ltd.
Toyohashi, Japan

Y. Saijo
Tohoku University
Sendai, Japan

Abstract—**We have proposed a new method for two-dimensional acoustic impedance imaging for biological tissue that can perform micro-scale observation without slicing the specimen. A tissue was placed on a plastic plate of 0.5 mm in thickness. An acoustic pulse with a frequency range up to 100 MHz was transmitted from the "rear side" of the plate, the acoustic beam being focused at the boundary between the tissue and plate. The reflection intensity was interpreted into local acoustic impedance of the target tissue. An acoustic impedance microscopy with 200 x 200 pixels, its field of view being 2 x 2 mm, was obtained by mechanically scanning the transducer. Quantification of acoustic impedance was performed using water or an appropriate material as a reference. The accuracy was evaluated using saline with various NaCl content. A rat cerebellum was employed as the specimen. The development of parallel fiber in cerebella cultures was clearly observed as the contrast in acoustic impedance. The proposed technique is believed to be a powerful tool for biological tissue characterization, as neither staining nor slicing is required.**

Keywords: biological tissue; acoustic impedanc; micro-scale imaging.

I. INTRODUCTION

In most of optical observation of biological tissue, the specimen is sliced into several micrometers in thickness, and fixed on a glass substrate. The microscopy is obtained by transmitted light through the specimen. As it is normally not easy to get a good contrast by local difference in refraction and/or transmission spectrum, the specimen is usually stained before being observed. It can be classified as a kind of chemical imaging, since only a portion that has a specific chemical property can be stained by selecting an appropriate staining material. However, the staining has some disadvantages. It normally takes from several hours to several days to finish the process. Furthermore, the tissue, after being stained, often completely loses its biological functions; i.e., the observation with staining process is chemically destructive.

On the other hand, acoustic imaging can be performed without staining process; i.e., it is chemically non-destructive. The observation can be finished in a very short time, as it does not need the staining process. The idea of ultrasonic microscopy for biological tissue is based on this advantage, and it is considered to become a powerful tool for tissue characterization that can image elastic parameters. Most of ultrasonic microscopes are scanning type, in which the response to a focused acoustic signal is successively acquired as the beam is mechanically scanned [1-2].

The authors previously proposed a pulse driven ultrasonic sound speed microscopy that can obtain sound speed image in a short time [3-4]. Although a small roughness of the specimen was approved in this type of microscope, slicing the specimen into several micrometers was still required for the observation. However it is often required that the observation can be performed without slicing process, as slicing may damage some functions of the tissue.

Based on the above background, the authors have newly proposed the acoustic impedance microscopy that can image the local distribution of cross sectional acoustic impedance of tissue. As acoustic impedance is given as a product of sound speed and density, it would have a good correlation with sound speed, when the variance in density was not significant. In this paper, the methodology of micro-scale imaging of cross sectional acoustic impedance and its accuracy will be described. As one of the applications, the paper will deal with the observation of cerebellar tissue of a rat.

II. SAMPLE PREPARATION

The cerebellum tissue of a rat was employed as the specimen to be observed. Rats were dissected, and their whole brains were removed. The isolated cerebellums were thickly sliced for both acoustic and optical observations. The 200 μm-thick slices were incubated in oxygenated phosphate buffer solution (PBS) on ice for one hour. They were chemically fixed with 4% formaldehyde fixative, for 20 minutes. For optical observation, some slices were subjected to immunohistochemical staining against calbindin D-28k. The slices were rinsed and observed in same PBS.

The substrate was a flat plastic plate made of polymethylmetacrylate (PMMA), its thickness being 0.5 mm. A reference material, of which acoustic impedance was known, was placed on the same substrate. In many cases, the target tissue was observed together with the reference, in the same field of view.

In this report, a silicone rubber, distilled water or agar was employed as a reference material, choosing one of them depending on the convenience of the measurement. In case of

using silicone rubber, the observation was performed after having waited for more than 24 hours since the rubber had been hardened, in order to retain the stability of the material.

III. EXPERIMENTAL SETUP

Fig. 1 illustrates the outline of the acoustic impedance microscope. Distilled water was used for the coupling medium between the substrate and transducer. A sharp electric pulse of about 40 V in peak voltage and 2 ns in width was generated by the pulse generator (AVTEC, AVP-AV-HV3-C). The maximum repetition rate of the pulse was as high as 10 kHz. The transducer was PVDF-TrFE type. It was 1.5 mm in aperture diameter, and 3.0 mm in focal length. An acoustic wave with a wide frequency component was generated by applying the voltage pulse. The acoustic wave, being focused on the interface between the substrate and tissue, was transmitted and received by the same transducer.

The reflection was detected and digitized by the oscilloscope (Tektronix, TDS-7145B). Considering the focal distance and the sectional area of the transducer, the diameter of the focal spot was estimated to be about 50 μ m at 80 MHz. The distance between the nearest two points was typically set at 10 μ m. Two-dimensional profile of acoustic impedance was obtained by mechanically scanning the transducer using the stage driver, keeping the focal point on the rear surface of the substrate. A typical field of view of 2 mm x 2 mm was covered with 200 x 200 pixels. It took typically 2 - 3 minutes for one observation. In order to save the time for data transfer from the oscilloscope to computer, the waveforms through each X-scan were once stored in the oscilloscope using its fast-frame mode before being transferred through the LAN interface. In order to reduce random noise, three times of responses at the same point were averaged. All the measurements were performed at room temperature.

IV. RESULTS

A. Waveforms

Figure 2 shows the acoustic signal from the reference material. A water droplet was used as the reference. The signal from the target tissue was very similar in waveform but slightly smaller than that from the reference, suggesting the acoustic impedance of the tissue was slightly higher than that of water (1.5×10^6 Ns/m^3). Frequency domain analysis showed that the spectrum was widely spread between 30 - 100 MHz within -12 dB.

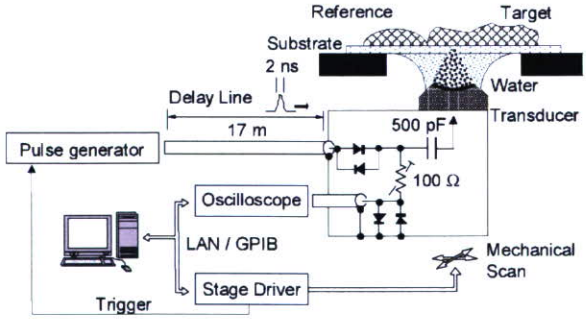

Fig. 1. Schematic diagram of the system.

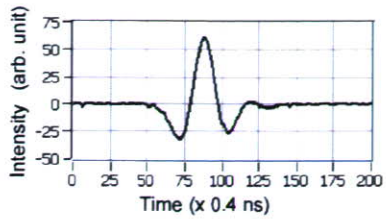

Fig. 2 A reflected acoustic signal.

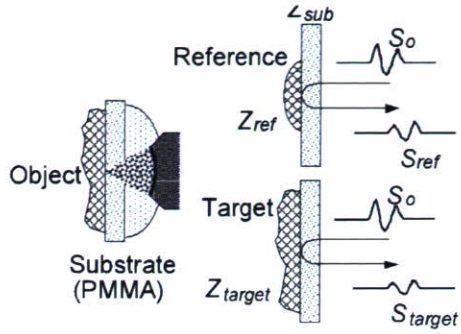

Fig. 3. Illustration for calibration of the acoustic impedance.

B. Calibration

Figure 3 illustrates the calibration of acoustic impedance. The target signal is compared with the reference signal. Hereafter, the signal component at an arbitrary frequency will be symbolized by S. Considering the reflection coefficient, the target signal S_{target} can be described as

$$S_{target} = \frac{Z_{target} - Z_{sub}}{Z_{target} + Z_{sub}} S_0 \qquad (1),$$

where S_0 is the transmitted signal, Z_{target} and Z_{sub} are the acoustic impedances of the target and substrate, respectively. On the other hand, the reference signal can be described as

$$S_{ref} = \frac{Z_{ref} - Z_{sub}}{Z_{ref} + Z_{sub}} S_0 \qquad (2),$$

where Z_{ref} is the acoustic impedance of the reference material. We can measure S_{target} and Z_{ref}, however, cannot directly measure S_0. The acoustic impedance of the target is subsequently calculated as a solution of the simultaneous equations for Z_{target} and S_0, as

$$Z_{target} = \frac{1 - \frac{S_{target}}{S_0}}{1 + \frac{S_{target}}{S_0}} Z_{sub} = \frac{1 - \frac{S_{target}}{S_{ref}} \cdot \frac{Z_{sub} - Z_{ref}}{Z_{sub} + Z_{ref}}}{1 + \frac{S_{target}}{S_{ref}} \cdot \frac{Z_{sub} - Z_{ref}}{Z_{sub} + Z_{ref}}} Z_{sub} \qquad (3),$$

assuming that S_0 is constant throughout the observation process.

In case of using water as the reference, its acoustic impedance was assumed to be 1.5 x 10^6 Ns/m^3. On the other hand, in case of using silicon rubber, the acoustic impedance of itself was calibrated, by using water as the standard reference material. In this report, 0.985 x 10^6 Ns/m^3 was used. The acoustic impedance of agar was calibrated in the same manner short time before the observation. It was calculated to be 1.65 x 10^6 Ns/m^3.

As the sound speed of the substrate at 80 MHz at 25 °C and its density at 25 °C were 2.78 km/s and 1.16 mg/mm^3, respectively, its acoustic impedance was calculated to be 3.22 x 10^6 Ns/m^3.

C. Evaluation of accuracy

In order to evaluate the accuracy of acoustic impedance, droplets of saline with different NaCl contents were prepared. Their acoustic impedance was measured using a droplet of distilled water as the reference.

The intensity of the reflected signal was lower with higher acoustic impedance, as the acoustic impedance of the droplets was lower than that of the substrate. The lower signal intensity was subsequently converted into higher acoustic impedance.

Figure 4 shows the result. Each plot represents the average of 600 points, the length of error bar indicating twice the standard deviation. It is seen that the acoustic impedance gradually increases with increasing NaCl content. The dotted curve represents the acoustic impedance as the product of sound speed and density. It agrees well with the measured result. Considering that the acoustic impedance of most of soft biological tissues is distributed between 1.5 - 1.8 x 10^6 Ns/m^3, the result suggests that the accuracy satisfies the requirement for tissue characterization.

D. Observation of cerebellar cortex of a rat

Figure 5 illustrates the development of cerebellar cortex [5-6]. Parallel fibers in molecular layer are axons of granule cells and play an important role in cerebella neuronal connections. Migrating granule cells elongate them horizontally and form

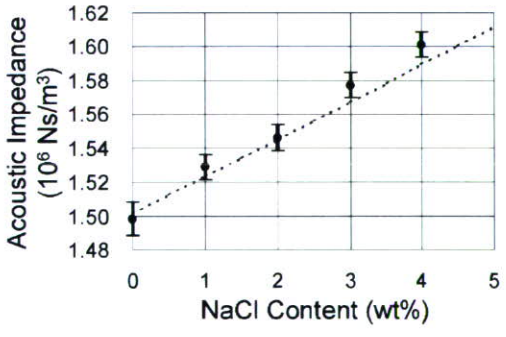

Fig. 4 Acoustic impedance of salt water as a function of NaCl content. Dotted curve indicates the product of sound speed and density.

many excitatory synapses to dendrites of Purkinje cells. These are major neuronal circuits of cerebellum so that parallel fibers are expected to construct rich molecular layer with development. However, it was hard to evaluate a degree of parallel fiber development with over molecular layer. We have little sufficient histochemical tools to visualize the developing parallel fibers.

Figure 6 shows the observed images of cerebellar cortex of a rat at immature (P1; postnatal 1 day), transient (P7), and mature (P20) stages. All the specimens in Fig. 6 had been chemi-

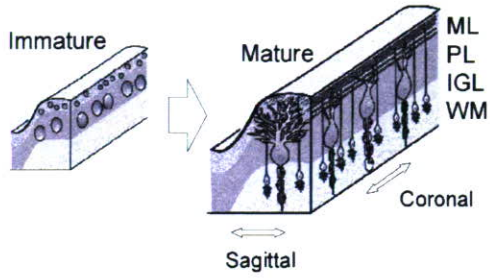

Fig. 5 Illustration for the development of cerabellar cortex.

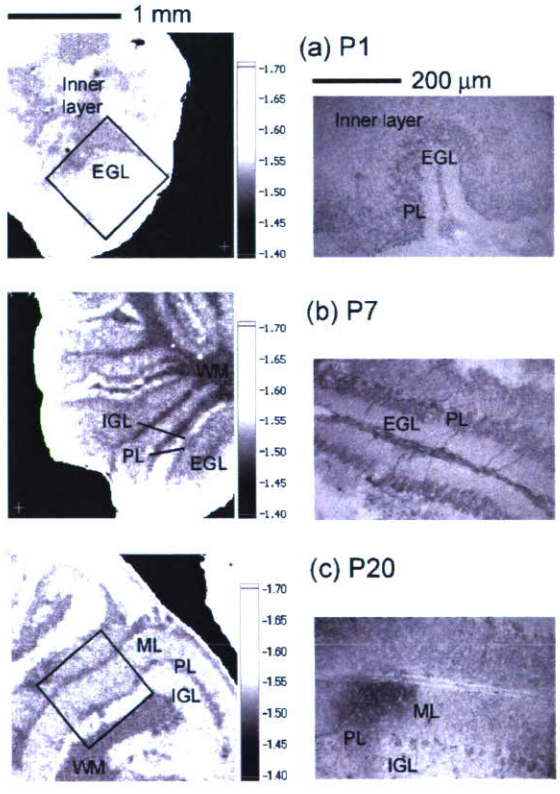

Fig. 6 Two-dimensional profiles of acoustic impedance (x 10^6Ns/m^3) of cerebellar cortex (left) and optical microscopy (right). Specimen: rat, sagittal cross section, chemically fixed. Frequency range: 60-100 MHz.

cally fixed.

In the immature cerebellar cortex (P1), the external granular layer (EGL), the outer layer of the cortex, showed higher impedance compared to the inner layer. The area indicated by the rectangle in the acoustic image is morphologically corresponding to the immunohistochemical observation, although the scale is not completely corresponded because the tissue was somehow subjected to compression during the acoustic observation. At this stage, as myelin is not yet generated, the existence of white matter (WM) is not clearly observed.

In the transient stage, four different layers, the WM, internal granular layer (IGL), Purkinje layer (PL) and EGL become to be comprehensive. The EGL and IGL showed higher impedance than the PL and WM. Morphological correspondence between acoustic and immunohistochemical observation is however not clear in these images.

In the mature stage, the EGL, which is composed of small neuronal cell bodies, has developed into the molecular layer (ML), which is composed of elongated axon (neurite), called parallel fibers. The four layers, WM, IGL, PL and ML are more clearly observed in acoustic image. The correspondence with immunohistological observation is also clearly seen.

It should be noted that very similar images were observed by simply contacting a cross section of the whole tissue with the substrate, without performing chemical fixation.

V. DISCUSSION

Considering the precision of the calibration, the reference material should be stable in both physical and chemical properties, and should strongly adhere to the substrate. It is recommended that the acoustic impedance of the reference be close to that of the target. Furthermore, as for the substrate, most of available materials have higher acoustic impedance than biological tissues. In such cases, the phase of the transmitted signal is reversed at the interface. The acoustic impedance of the substrate should be sufficiently high compared to that of the target, in order to retain a strong reflection. However extremely high acoustic impedance of the substrate may increase the reflection coefficient at the interface between the coupling medium and substrate, and reduce the intensity of transmitted signal to the target. This would obviously reduce the S/N ratio. Therefore, in order to obtain a good S/N ratio, the materials should be carefully selected considering their accordance.

As the transducer was designed for usage with water as the coupling medium, the existence of the plastic plate between the transducer and focal point may bring an aberration. This will be significant if the thickness of the substrate is very thick, and the convergence angle is very large. In this experiment, however, the angle was as small as 4.4 degrees, suggesting the error brought by the aberration would be small. Nevertheless, a quantitative analysis is needed in order to precisely assess the acoustic impedance, especially when a thick substrate is employed.

As the WM is rich with fat, its acoustic impedance would be lower than the IGL. The ML is composed of axon, which has many actin fibers with high elasticity [7]. It would lead to high acoustic impedance. The reason why the Purkinje layer has low impedance is, however, not clear. Further pharmacological investigation is required.

VI. SUMMARY

A new method for two-dimensional acoustic impedance imaging for biological tissue characterization with micro-scale resolution was proposed. Calibration was performed using a reference material of which acoustic impedance was known. Quantitative imaging of acoustic impedance was made possible. Acoustic impedance microscopy with 200 x 200 pixels, its typical field of view being 2 x 2 mm, was obtained by scanning the transducer. Its accuracy, evaluated using saline with various NaCl content, was of satisfactory for characterization of soft tissues. The development of cerebella cultures of a rat was clearly observed as the contrast in acoustic impedance, without staining the specimen. The technique is believed to be a powerful tool for biological tissue characterization, as neither staining nor slicing is required.

ACKNOWLEDGEMENTS

The authors would like to express their sincere thanks to C-K. Lee, T. Morishima and E. Fukushi of Toyohashi University of Technology for their assistance with the experiment. This study was financially supported by Grants-in-Aid for Scientific Research (Scientific Research (B)15360217, (B) 15300178), and Japan Society for the Promotion of Science and Health and Labor Sciences Research Grants from the Ministry of Health, Labor and Welfare for the Research on Advanced Medical Technology (H17-Nano-001).

REFERENCES

[1] Y. Saijo, M. Tanaka, H. Okawai, H. Sasaki, S. Nitta & F. Dunn: "Ultrasonic Tissue Characterization of Infarcted Myocadium by Scanning Acoustic Microscopy", *Ultrasound in Med. & Biol.*, 23-1, 77 (1997).

[2] H. Okawai, K Kobayashi & S. Nitta: "An Approach to Acoustic Properties of Biological Tissues Using Acoustic Microgfraphs of Attenuation Constant and Sound Speed", *J. Ultrasound Med.*, 20, 891 (2001).

[3] N. Hozumi, R. Yamashita, C-K Lee, M. Nagao, K. Kobayashi, Y. Saijo, M. Tanaka, N. Tanaka & S Ohtsuki: "Ultrasonic Sound Speed Microscope for Biological Tissue Characterization Driven by Nanosecond Pulse", *Acoustic Science & Technology*, 24, 386 (2003).

[4] N. Hozumi, R. Yamashita, C-K. Lee, M. Nagao, K. Kobayashi, Y. Saijo, M. Tanaka, N. Tanaka & S.Ohtsuki: "Time –frequency analysis for pulse driven ultrasonic microscopy for biological tissue characterization", *Ultrasonics*, 42, 717 (2003).

[5] D. H. Sanes, T. A. Reh & W. A. Harris: *Development of the Nervous System*, Academic Press (2000).

[6] E. R. Kandel, J. H. Schwarts & T. M. Jessell: *Principles of Neural Science*, McGraw-Hill (2000).

[7] HW. Wu, T. Kuhn & VT. Moy: "Mechanical Properties of L929 Cells Measured by Acoustic Force Microscopy: Effects of Anticytoskeltal Drugs and Membrane Crosslinking", *Scanning*, 20, 389 (1998).

Speed of Sound Microscopy for Biomedical Applications

Y. Saijo, H. Sasaki, T. Yambe, M. Tanaka
Department of Medical Engineering and Cardiology
Institute of Development, Aging and Cancer, Tohoku University
4-1 Seiryomachi, Aoba-ku, Sendai 980-8575, Japan
saijo@idac.tohoku.ac.jp

N. Hozumi
Department of Electrical and Electronic Engineering
Graduate School, Toyohashi University of Technology
1-1 Tempaku, Toyohashi, 441-8580, Japan

K. Kobayashi, N. Okada
Research & Development Headquarters
Honda Electronics Co. Ltd.
20 Oyamazuka, Oiwa-cho, Toyohashi, 441-3193, Japan

Abstract — **We have been developing a scanning acoustic microscope (SAM) system for medicine and biology featuring quantitative measurement of ultrasonic speed and attenuation of soft tissues. In the present study, we will propose a new concept ultrasonic speed microscopy that can measure the thickness and ultrasonic speed using fast Fourier transform of a single pulsed wave instead of continuous waves used in conventional SAM systems. Six coronary arteries were frozen and sectioned approximately 10 μm in thickness. They were mounted on glass slides without cover slips. The scanning time of a frame with 300×300 pixels was 90 s and two-dimensional distribution of speed of sound was obtained. The speed of sound was 1720 m/s in the thickened intima with collagen fiber, 1520 m/s in lipid deposition underlying fibrous cap and 1830m/s in calcified lesion in the intima. These basic measurements will help understanding echo intensity and pattern in intravascular ultrasound (IVUS) images.**

Keywords; acoustic microscopy, ultrasonic speed, coronary artery, atherosclerosis

I. INTRODUCTION

We have been developing a scanning acoustic microscope (SAM) system for biomedical use since 1985. We have been investigating the acoustic properties of various organs and disease states by using this SAM system. In the areas of medicine and biology, scanning acoustic microscopy (SAM) has three main objectives. The first, SAM is useful for intraoperative pathological examination because it doesn't require a special staining. The second, SAM provides basic data for understanding lower frequency medical ultrasound images such as echocardiography or intravascular ultrasound. The third, SAM can be used to assess biomechanics of tissues and cells at a microscopic level. The originality of the previous SAM system of Tohoku University lies in providing quantitative values of attenuation and speed of sound in thin slices of soft tissue. Although the system may be currently in use, it was constructed using precise hand-crafted technologies and analog signal acquisition circuits. Besides, the previous system needed repeated acquisitions for calculation of quantitative values because it used continuous waves of different frequencies.

Recently, we have proposed a prototype of speed of sound microscopy using a single pulsed wave instead of continuous waves used in conventional SAM systems. In the present study, we construct a compact, commercially available speed of sound microscopy and evaluate the system performance by measuring normal and atherosclerotic coronary arteries.

II. METHODS

A. Tissue Preparation

Normal and atherosclerotic human coronary arteries were obtained from autopsy. The specimens were rinsed in PBS (phosphate buffer saline) and immersed in 10% to 30% sucrose solutions. Then the specimens were embedded in OCT (optimal cutting temperature) compound and rapidly frozen by liquid nitrogen at –20°C. The specimens were sliced approximately 10 microns by a cryostat and mounted on a silane-coated glass slides.

B. *Speed of Sound Microscopy*

Fig. 1 shows a block diagram of speed of sound microscopy for biological tissue characterization. A single ultrasound pulse with a pulse width of 6 ns was emitted and received by the same transducer above the specimen. The aperture diameter of the transducer was 1.2 mm, and the focal length was 1.5 mm. The central frequency was 80 MHz, the bandwidth was 40-150 MHz, and the pulse repetition rate was 10 kHz. The diameter of the focal spot was estimated to be 20 μm at 80 MHz by taking into account the focal distance and sectional area of the transducer. Distilled water was used as the coupling medium between the transducer and the specimen. The reflections from the tissue surface and those from the interface between the tissue and glass were received by the transducer and were introduced into a Windows-based PC (Pentium 4, 2.8 GHz, 1GB RAM, 80GB HDD) via an analogue-digital converter (Acqiris DP-210, Geneva, Switzerland). The frequency range was 500 MHz, and the sampling rate was 2 GS/s. Eight values of the time taken for a pulse response at the same point were averaged in order to reduce random noise.

The transducer was mounted on an X-Y stage with a microcomputer board that was driven by the PC through RS232C. The Both X-scan and Y-scan were driven by linear servo motors. Finally, two-dimensional distributions of ultrasonic intensity, speed of sound, attenuation coefficient and thickness of a specimen measuring 2.4×2.4 mm were visualized using 300×300 pixels. The total scanning time was 90 s.

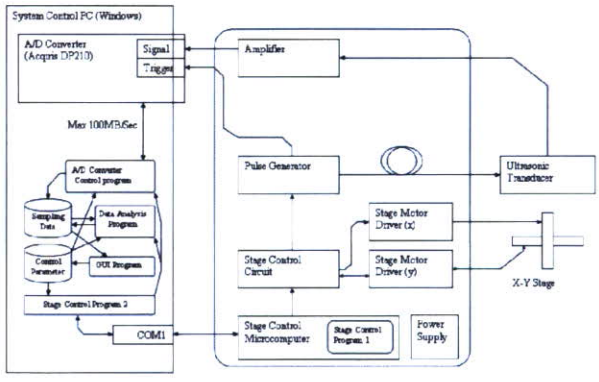

Figure 1. Block diagram of speed of sound microscopy.

Fig. 2 shows the appearance of the speed of sound microscopy. Whole system are on the desktop.

Figure 2. Apperance of the speed of sound microscopy.

C. *Signal Analysis [10]*

The reflected waveforms are shown in Fig. 3. The waveform at the glass surface without the tissue is shown in (a). This signal was used as a reference waveform. The decline of the glass surface was compensated by measuring three different points in the glass area surrounding the tissue. The waveform from the tissue area is shown in (b). Although the waveform contains two reflections at the surface and at the interface of the tissue and glass, the two components cannot be separated in time domain analysis. Thus, frequency domain analysis was performed by analyzing the interference between the two reflections. Intensity and phase spectra were calculated by Fourier transforming the waveform. The spectra were normalized by the reference waveform. Fig. 4 shows the frequency domain analysis of the interfered waveform.

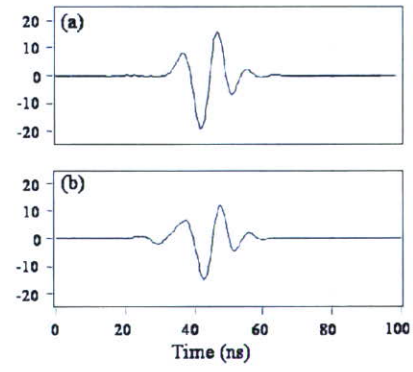

Figure 3. Reflected waveforms (a) from the glass surface without tissue, and (b) from the tissue area

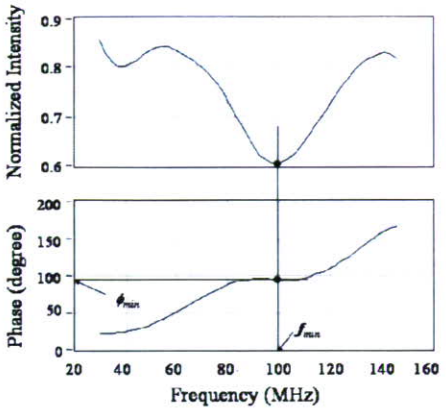

Figure 4. Frequency domain analysis of interfered waveform. f_{min}: the minimum point in the intensity spectrum, ϕ_{min}: corresponding phase angle

Denoting the minimum point in the intensity spectrum by f_{min} and the corresponding phase angle by ϕ_{min}, the phase difference between the two reflections at the minimum point is $(2n-1)\pi$, which yields

$$2\pi f_{min} \times \frac{2d}{c_o} = \phi_{min} + (2n-1)\pi \qquad (1)$$

where d, c_o, and n are the tissue thickness, speed of sound in water, and a non-negative integer, respectively.

The phase angles ϕ_{min} can be expressed by

$$2\pi f_{min} \times 2d\left(\frac{1}{c_o} - \frac{1}{c}\right) = \phi_{min} \qquad (2)$$

since ϕ_{min} is the phase difference between the wave that travels the distance $2d$ with speed of sound c and the wave that travels a corresponding distance with speed of sound c_o. By solving equations (1) and (2),

$$d = \frac{c_o}{4\pi f_{min}}\{\phi_{min} + (2n-1)\pi\} \qquad (3)$$

is obtained for the minimum point.

Finally, the speed of sound at each frequency is calculated as

$$c = \left(\frac{1}{c_o} - \frac{\phi_{min}}{4\pi f_{min} d}\right) \qquad (4)$$

After determination of the thickness, attenuation of ultrasound was then calculated by dividing amplitude by the thickness and frequency.

III. RESULTS

Fig. 5 shows a PC window of our ultrasonic speed microscopy. The upper left is an amplitude image, the upper right is an ultrasonic speed image, the lower left is an attenuation image and the lower right is the thickness distribution of the normal coronary artery. The intima is thin and speed of sound is 1600 m/s in the intima, 1560 m/s in the media and 1590 m/s in the adventitia, respectively.

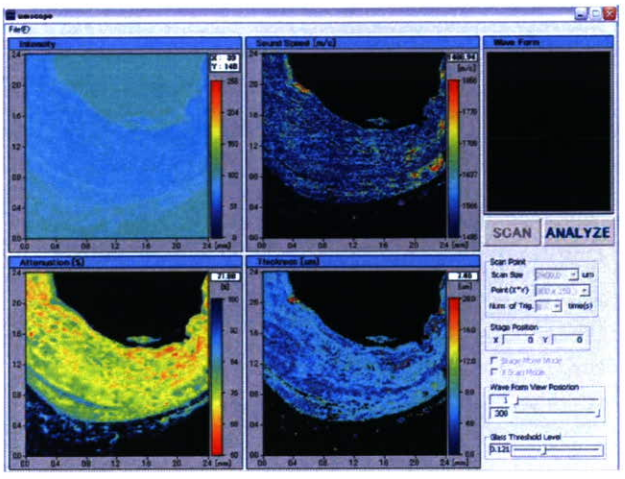

Figure 5. PC window of speed of sound microscopy showing a normal coronary artery. Upper left: amplitude image, upper right: speed of sound image, lower left: attenuation image and lower right: thickness

Fig. 6 is an atherosclerotic coronary artery. The speed of sound is 1680 m/s in the thickened intima with collagen fiber, 1520 m/s in lipid deposition underlying fibrous cap and 1810m/s in calcified lesion in the intima.

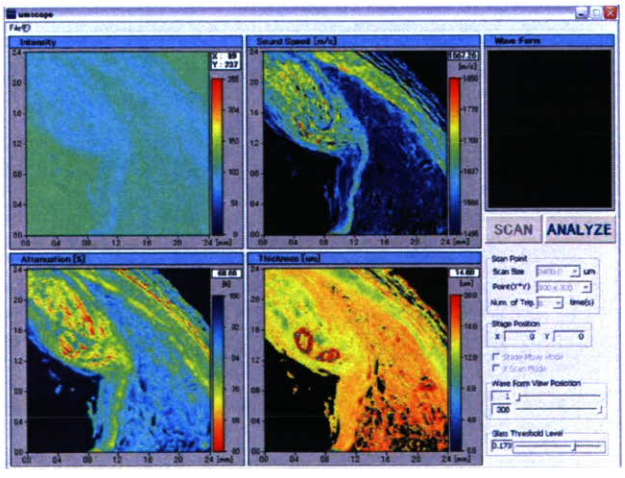

Figure 6. PC window of speed of sound microscopy showing an atherosclerotic coronary artery. Upper left: amplitude image, upper right: speed of sound image, lower left: attenuation image and lower right: thickness.

IV. Discussion

In the present study, speed of sound in the excised human coronary arteries was measured with the ultrasonic speed microscopy. The results would become basic data base for interpretation of clinical IVUS images and novel IVUS imaging technologies.

The results showed that the speed of sound in the intima and adventitia, mainly consisted of collagen fiber, had higher values than those of media, mainly consisted of vascular smooth muscle. The different of acoustic properties may lead to the classical three-layered appearance of normal coronary artery in clinical IVUS imaging. The findings indicate that the echo intensity is not determined by the difference of acoustic impedance between neighboring layers. The distribution and the structure of materials with different acoustic properties may also contribute to the echo pattern in IVUS.

The plaque with a thick fibrous cap consisted of collagen fiber, considered showed higher value of speed of sound than those of normal media. Generally, absorption and scattering are the two main factors of attenuation of ultrasound. Thus, the high scattering within the thickened intima may lead to the high intensity echo in the "hard plaque". Lipid showed speed of sound. These values explain the low echo in the "soft plaque" in the same manner of renal cysts containing water like fluid. Besides its absolute low values, the homogeneity of acoustic properties within the lipid pool may contribute to the low scattering and consequently a lipid pool shows low intensity echo.

V. Conclusions

An acoustic microscope system that can measure the speed of sound of thin slices of biological material was developed. It was a unique acoustic microscope because it used a single pulse and the Fourier transform to calculate the speed of sound at all measuring points. Although the data acquisition time of a single frame was greater than that in conventional SAM, the total time required for calculation was significantly shorter. The acoustic microscope system can be applied to intraoperative pathological examination..

Acknowledgments

This study was supported by Grants-in-Aid for Scientific Research (Scientific Research (B) 15300178, Scientific Research (B) 15360217) from the Japan Society for the Promotion of Science and Health and Labor Sciences Research Grants from the Ministry of Health, Labor and Welfare for the Research on Advanced Medical Technology (H17-Nano-001).

References

[1] Y. Saijo, M. Tanaka, H. Okawai, F. Dunn, The ultrasonic properties of gastric cancer tissues obtained with a scanning acoustic microscope system, Ultrasound Med Biol 17 (1991), pp. 709-714.

[2] H. Sasaki, M. Tanaka, Y. Saijo, H. Okawai, Y. Terasawa, S. Nitta, K. Suzuki, Ultrasonic tissue characterization of renal cell carcinoma tissue, Nephron 74 (1996), pp. 125-130.

[3] Y. Saijo, M. Tanaka, H. Okawai, H. Sasaki, S. Nitta, F. Dunn, Ultrasonic tissue characterization of infarcted myocardium by scanning acoustic microscopy, Ultrasound Med Biol 23 (1997), pp. 77-85.

[4] Y. Saijo, H. Sasaki, H. Okawai, S. Nitta, M. Tanaka, Acoustic properties of atherosclerosis of human aorta obtained with high-frequency ultrasound, Ultrasound Med Biol 24 (1998), pp. 1061-1064.

[5] Y. Saijo, H. Sasaki, M. Sato, S. Nitta, M. Tanaka, Visualization of human umbilical vein endothelial cells by acoustic microscopy, Ultrasonics 38 (2000), pp. 396-399.

[6] Y. Saijo, T. Ohashi, H. Sasaki, M. Sato, C.S. Jorgensen, S. Nitta, Application of scanning acoustic microscopy for assessing stress distribution in atherosclerotic plaque, Ann Biomed Eng 29 (2001), pp. 1048-53.

[7] H. Sasaki, Y. Saijo, M. Tanaka, S. Nitta, Influence of tissue preparation on the acoustic properties of tissue sections at high frequencies, Ultrasound Med Biol 29 (2003), pp. 1367-72.

[8] Y. Saijo, T. Miyakawa, H. Sasaki, M. Tanaka, S. Nitta, Acoustic properties of aortic aneurysm obtained with scanning acoustic microscopy, Ultrasonics 42 (2004), pp. 695-698.

[9] H. Sano, Y. Saijo, S. Kokubun, Material properties of the supraspinatus tendon at its insertion – A measurement with the scanning acoustic microscopy, J. Musculoskeletal Res. 8 (2004), pp. 29-34.

[10] N. Hozumi, R. Yamashita, C.K. Lee, M. Nagao, K. Kobayashi, Y. Saijo, M. Tanaka, N. Tanaka, S. Ohtsuki, Time–frequency analysis for pulse driven ultrasonic microscopy for biological tissue characterization, Ultrasonics 42 (2004), pp. 717-722.

Coronary Plaque Classification through Intravascular Ultrasound Radiofrequency Data Analysis Using Self-organizing Map

Takahiro Iwamoto[1], Akira Tanaka[2], Yoshifumi Saijo[3], and Makoto Yoshizawa[4]
[1] Graduate School of Engineering, Tohoku University, Sendai, JAPAN
[2] Faculty of Symbiotic Systems Science, Fukushima University, Fukushima, JAPAN
[3] Institute of Development, Aging and Cancer, Tohoku University, Sendai, JAPAN
[4] Information Synergy Center, Tohoku University, Sendai, JAPAN

Abstract— **Intravascular ultrasound (IVUS) is an important clinical tool in the assessment of atherosclerotic plaque in coronary artery diseases. Using IVUS, we can obtain high resolution echo image of cross-sections of the coronary artery. However, it is difficult to accurately classify plaques by using the echogram only. We propose a method of IVUS Radiofrequency (RF) signal classification using self-organizing map (SOM). Characteristic ROIs (region of interest) of the IVUS echogram of patients with coronary lesions were selected by an expert medical doctor, and the SOM learned from these ROIs. The SOM could classify the RF signals with accuracies of 95.9% for fibrous plaque, 99.5% for blood, 96.2% for calcified plaque and 16.3% for media regions. This result suggests that the proposed technique is useful for automatic characterization of plaque in coronary artery.**

Keywords-; Intravascular ultrasound, Self organizing map, tissue characterization, Spectrum analysis

I. INTRODUCTION

Rupture of vulnerable atherosclerotic plaque is the cause of most acute coronary syndromes.

Accurate *in vivo* identification of plaque components may allow the detection of vulnerable atheroma before rupture. IVUS allows the visualization of cross-sections of coronary artery with atherosclerotic plaques *in vivo* [1]-[5]. In standard IVUS gray-scale images, calcified plaque regions and dense fibrous components generally reflect ultrasound energy well and thus appear bright and homogeneous in IVUS images. They are usually labeled as "hard" plaque. Conversely, regions of low echo reflectance in IVUS images are usually labeled as "soft" plaque [6]. However, the visual interpretation is limited in the assessment of quantitative plaque composition. But, spectral analysis of the radiofrequency (RF) ultrasound signals may allows detailed assessment of plaque composition.

Therefore, the goal of this study was to compare real-time determination of plaque components, using easily accessible IVUS backscattered signals. With the use of a combination of spectral parameters, classification schemes were developed for the analysis of IVUS data, and the RF spectral information was used to reconstruct tissue maps.

II. METHOD

RF Signal data were acquired from 14 human left anterior descending (LAD) coronary arteries at PTCA (percutaneous transluminal coronary angioplasty). The average age was 72 ± 12 years.

A. Data Acquisition

IVUS data were acquired with an IVUS console "Clear View Ultra" (Boston Scientific Inc, USA) and 40MHz, mechanically rotating IVUS catheter "Atlantis SR Plus" (Boston Scientific Inc, USA).

RF data were digitized and stored in a PC (Dell Precision Workstation 330, Dell Inc, USA) using an A/D board "GAGE compuscope 8500" (500Msamples/sec., with 8 bits of resolution, Gage Applied Inc, Montreal, Canada) for off-line analysis.

B. IVUS Data Analysis

IVUS RF signal from the ROIs selected by the expert medical doctor were processed in MATLAB 6.5 (The MathWorks Inc, USA) as follows.

Initially, a band-pass filter (15MHz-105MHz) was applied to the IVUS RF signal data. Then each line in the ROI is scanned by a 128-points width hamming window. The frequency spectrum is calculated for each position of the hamming window using a mathematical autoregressive (AR) model

AR processes are known to be more appropriate for short data records, such as IVUS signals, than discrete Fourier

Acknowledgements: This study was supported by Grants-in-aid from Japan Society of Promotion of Science (15300178) and Grants-in-aid from Ministry of Health, Labour and Welfare (H17-nano-001).

transforms and have been shown to result in high resolution spectral estimates [7].

Preliminary tests in this study estimated the optimum AR model order (order 15 via Akaike's final prediction error method [8]) for characterizing plaque components, after tests with several models.

Further, the optimized AR spectra were used to compute 18 spectral shape parameters for each ROI. These parameters were: fundamental wave power, frequency of fundamental wave power, second harmonic wave power, frequency of harmonic wave power, local minimum power between fundamental wave power and second harmonic wave power, frequency of local minimum power, maximum power, frequency of maximum power, slope from power at frequency 15MHz to fundamental wave power, corresponding y-intercept, slope from fundamental wave power to local minimum power, corresponding y-intercept, slope from local minimum power to second harmonics power, corresponding y-intercept, slope from second harmonics power to 100MHz power, corresponding y-intercept, mean of integrated backscatter, ROI position at line.

C. *Training data and test data*

ROIs for training data and test data were selected from IVUS B-mode images by an expert medical doctor. These IVUS B-mode images were reconstructed from the RF data by software written by our group. Then three plaque types (fibrous, calcified and other plaque) and four structure types (catheter, shade of guide-wire, blood, and media) were defined. 75% of these data were used as training data of the SOM classifier. The rest of these data was used as test data of the SOM classifier.

D. *SOM*

After the training, the SOM classifier was used to classify IVUS RF signals.

The SOM is a neural network based on unsupervised learning proposed by T. Kohonen [9]. It is a vector quantization method which places the prototype vectors on a regular low-dimensional grid in an ordered fashion. This makes the SOM a powerful visualization tool. A SOM consists of neurons organized on a regular low-dimensional grid. Each neuron is a d-dimensional weight vector (prototype vector, codebook vector) where d is equal to the dimension of the input vectors.

The neurons are connected to adjacent neurons by a neighborhood relation, which dictates the topology, or structure, of the map.

E. *SOM Training Settings*

The SOM training settings were as follows.

Map size was 25 × 17 of hexagonal lattice (numbers of neuron was 425). Training phase was 20,000 times. A batch training algorithm was used, the data set were presented to the SOM as a whole, and the new weight vectors were weighted averages of the data vectors [10].

F. *Labeling Each neuron at SOM*

After training, the neurons of the SOM were labeled in accordance with the representatives vectors of the training data. Each label was decided based on the major component of the group.

Using this labeled SOM, the ROIs were classified.

G. *Plaque Classification*

The SOM classifier learned the plaque component type by using spectral parameters.

At each line in ROIs, frequency spectra of samples within the window were calculated, and spectral shape parameters were derived. The plaque types were classified based on these parameters.

The window was then moved by one sample, and data were reanalyzed.

Hence, each sample was given a particular value corresponding to one of the 7 components (catheter, shade of guide-wire, blood, calcified plaque, fibrous plaque, media, and other).

The results were validated through classifying data that were used in the SOM training to determine predictive accuracy, sensitivity, and specificity from widely accepted equations in biomedical literature [11].

Color codes were assigned to the plaque component values, and the tissue maps were reconstructed on IVUS B-mode images by our algorithm.

These tissue maps were then checked by an expert medical doctor to assess the plaque characterization.

III. RESULTS

Twenty-three plaque ROIs were identified in a group of 14 vessel images.

ROIs were selected by an expert medical doctor for catheter (n=21), shade of guide-wire (n=18), blood (n=15), fibrous

plaque (n=11), calcified plaque (n=31), and media (n=27) areas.

75% of these data are used as training data for the SOM, and the rest of these data are used as test data. The SOM learned from the AR spectrum parameters of training data. And the SOM was validated by classification of training data and test data.

The SOM learned from training data and each neuron of the SOM labeled from training data are showed in Figure 1. As shown figure 1, each kinds of training data are organizing one area. This result suggests the setting of training data was reasonable.

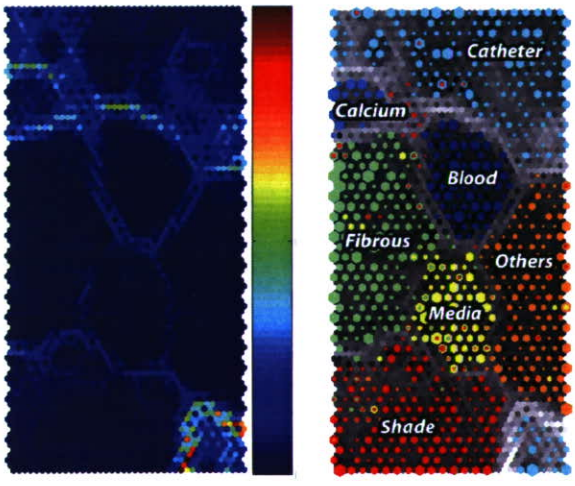

Figure 1. leaned SOM and labeld SOM

The sensitivity and specificity of classified training data by the SOM were showed in table I. There are high sensitivity and Specificity except media.

TABLE I. SENSITIVITY AND SPECIFICITY OF CLASSIFIED ROIS BY THE SOM(TRAINING DATA)

Kinds	Sensitivity	Specificity
Blood	100.0%	99.9%
Calcium	98.2%	100.0%
Catheter	99.8%	99.65%
Fibrous	94.2%	98.6%
Media	85.9%	98.4%
Others	97.0%	98.9%
Shade	89.8%	98.5%

The results of test data are showed in table II. Test data were not used as training data of SOM. So, classification of test data is the validation of the SOM classifier.

TABLE II. SENSITIVITY AND SPECIFICITY OF CLASSIFIED ROIS BY THE SOM(TEST DATA)

Kinds	Sensitivity	Specificity
Blood	100.0%	99.8%
Calcium	88.5%	99.8%
Catheter	99.2%	99.8%
Fibrous	88.3%	98.8%
Media	74.4%	96.7%
Others	92.8%	98.6%
Shade	88.3%	96.8%

Color-code map that classified whole echogram by the SOM is showed in figure 2 and figure 3. On the left hand side of figures 2 and 3 are the original echograms, and on the right hand side are color-code maps with the classification of each area of these echogram by the SOM.

In the figure 2, numbers of color bar are as follow: 1 is others, 2 is blood, 3 is fibrous plaque, 4 is shade of guide wire, 5 is blood, 6 is calcified plaque, 7 is media, and 8 is catheter. In the figure 3, numbers of color bar are as follow: 1 is catheter, 2 is others, 3 is shade of guide wire, 4 is blood, 5 is fibrous plaque, 6 is media, and 7 is calcified plaque.

The SOM classified well the inner lumen of figure 2, but not classified the outside of lumen. Because the SOM was not trained with data of outside of lumen.

The SOM did not classify well the image in the figure 3. In this image, the SOM classified area of inner lumen, media as fibrous plaque.

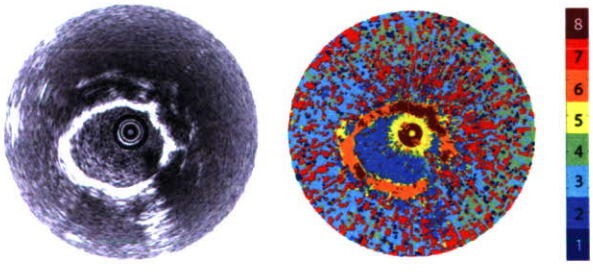

Figure 2. echogram and color-code map

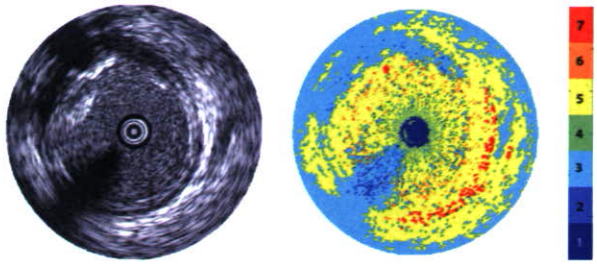

Figure 3. echogram and color-code map

IV. Conclusions

In this study, we classified IVUS RF data of coronary tissues using a SOM classifier based on multiple spectrum parameters.

The accuracies for classification of IVUS RF data were 95.9% for fibrous plaque region, 99.5% for blood region, 96.2 % for calcified plaque region, and 16.3 % for media regions. These results showed that the SOM classifier has potential for characterization of coronary tissues.

In future studies, with further data collection, we plan to develop statistically stable and robust classification rules for prediction of atherosclerotic plaque formation.

Acknowledgment

This study was supported by Grants-in-aid from Japan Society for Promotion of Science (15300178) and Grants-in-aid from Ministry of Health, Labour and Welfare (H17-nano-001).

References

] Klingensmith J, Vince D, Kuban B, et al. Assessment of coronary compensatory enlargement by three-dimensional intravascular ultrasound. Int J Card Imaging. 2000. vol.16. pp.87-98.

:] Nissen SE, Gurley JC, Grines CL, et al. Intravascular ultrasound assessment of lumen size and wall morphology in normal subjects and patients with coronary artery disease. Circulation. 1991. vol.84 pp.1087-1099.

;] Schoenhagen P, Ziada KM, Kapadia SR, et al. Extent and direction of arterial remodeling in stable versus unstable coronary syndromes. Circulation. 2000. vol.101. pp.598-603.

[4] Tuzcu EM, Hobbs RE, Rincon G, et al. Coronary heart disease/ myocardial infarction: occult and frequent transmission of atherosclerotic coronary disease with cardiac transplantation: insights from intravascularultrasound. Circulation. 1995. vol.91. pp.1706-1713.

[5] Von Birgelen C, de Vrey EA, Mintz GS, et al. ECG-gated threedimensional intravascular ultrasound: feasibility and reproducibility of the automated analysis of coronary lumen and atherosclerotic plaque dimensions in humans. Circulation. 1997. vol.96. pp.2944-2952.

[6] Nissen SE, Yock P. Intravascular ultrasound: novel pathophysiological insights and current clinical applications. Circulation. 2001. vol.103. pp. 604-616.

[7] Baldeweck T, Laugier P, Herment A, et al. Application of utoregressive spectral analysis for ultrasound attenuation estimation: interest in highly attenuating medium. IEEE Trans Ultrason Ferroelectrics Frequency Control. 1995;42:99–110.

[8] Kay SM. Modern spectral estimation. Theory and application. Englewood Cliffs, NJ: Prentice Hall, 1988.

[9] T.Kohonen, Self-Organizing Map, 3rd Edition, Springer, 2004.

[10] T. Kohonen, "New developments of learning vector quantization and the self-organizing map", SYNAPSE'92, Symposium on Neural Networks; Alliances and Perspectives in Senri 1992, Osaka, Japan, June 24–26, 1992.

[11] Metz CE. Basic principles of ROC analysis. Semin Nucl Med. 1978;8: 283–298.

Luminal Contour Detection in Intravascular Ultrasound Images

E. Santos Filho[1], M. Yoshizawa[2], A. Tanaka[3], Y. Saijo[4], T. Iwamoto[1]

1 Graduate School of Engineering, Tohoku Univ., Aoba 6-6-05, Aoba-ku, Sendai 980-8579, Japan

2 Information Synergy Center, Tohoku Univ., Aoba 6-6-05, Aoba-ku, Sendai 980-8579, Japan

3 College of Symbiotic Systems Science, Fukushima Univ., Kanayagawa 1, Fukushima 960-1296, Japan

4 Inst. of Development, Aging and Cancer, Tohoku Univ., Seiryo-machi, Sendai 980-8575, Japan

santos@yoshizawa.ecei.tohoku.ac.jp

Abstract: A system for luminal contour segmentation in intravascular ultrasound images is proposed. Moment based texture features together with the radial distance feature are used for clustering of the input image pixels. After the clustering, morphological smoothing and boundary detection process are applied and the final image is obtained. The proposed method was applied to 15 images of different patients and a correlation coefficient equal to 0.86 was obtained between the areas of lumen automatically and manually defined.

Keywords: image segmentation, texture, ultrasound.

1. Introduction

Cardiovascular pathologies are one of the main causes of mortality in the Western world. Atherosclerosis, disease of intima layer of the artery, represents the essential characteristic of arterial pathologies[1]. Atherosclerosis consists of lipids, complex carbohydrates, blood cells, fibrous tissues and calcified deposits, forming a plaque that occludes progressively the lumen of the artery. A number of imaging modalities exist to help diagnosis coronary artery diseases. Among them, X-ray coronary angiography and intravascular ultrasound (IVUS) represent the most commonly used diagnostic tools.

Segmentation of deformable structures is a common processing problem in medical imaging. For example, coronary artery atherosclerosis severity is mainly deduced from the degree of vessel stenosis induced by the atherosclerotic plaque formation. It is generally estimated, from IVUS images, by segmenting and measuring the lumen area, and by referencing it to the total cross-sectional area of the vessel. With the majority of IVUS systems, this work is generally performed manually. However, due to tedious nature of manual tracing, many research groups have worked on developing semi-automatic and automatic segmentation and analysis methods in IVUS images as well as angiography.

Brusseau *et al.*[2] developed a fully automatic method for luminal contour that evolves until it optimally separates regions with different statistical properties. Their system used a phase array transducer and achieved a high level of accuracy. However, no mention was made of the widely used rotating systems.

Bovenkamp *et al.*[3] developed an automatic multi-agent-based system for luminal contour segmentation. Each agent cooperates with other agents to come to a consistent overall image segmentation. However, the complexity of this system may lead to time delays when there is a conflict among the agents.

Tuceryan[4] proposed a method for obtaining texture features directly from gray-level images by computing the moments of the image in local regions. The results of his segmentation algorithm show that the image moments computed over local regions provide a powerful set of features that reflect certain textural properties in images.

In this papers, like those by Brusseau[2] and Bovenkamp[3], we proposed a system for automatic luminal contour segmentation. Unlike the Brusseau system,[2] our system is applied to images obtained from a rotating IVUS system due to the fact that these systems are widely used in clinical settings. Instead of a multi-agent system, as proposed by Bovenkamp[3], we used the simpler and more powerful set of features proposed by Tuceryan[4] to achieve our goal of luminal contour segmentation.

Our strategy to achieve this goal is to extract local moment based texture features and a pixel position feature from IVUS images to perform a clustering on the basis of these features. Once we obtain the clustered image, a smoothing filter is applied to reduce the irregularities of the boundary and then the final segmentation is carried out. This process is illustrated in Fig.1.

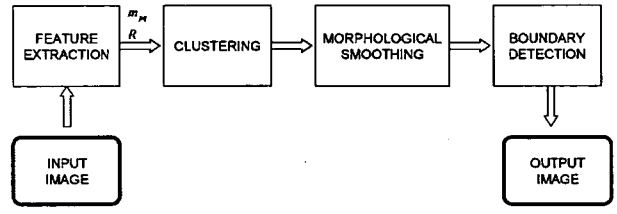

Fig.1 – Block diagram of the proposed system for luminal contour segmentation

PR0001/05/0000-1076 ¥400

2. Materials and Methods

Our texture segmentation algorithm is based on Tuceryan's work[4] and consists of the following steps: (a) compute the image moments within a small window around each pixel as well as the radial distance of each pixel, (b) compute the texture features from these moments by applying a nonlinear transformation followed by an averaging operation, (c) perform a fuzzy clustering of the pixels of the input image on the basis of these features, and (d) classify every pixel in the image according to the minimum distance from the centers of the clusters found in step (c).

In this system the input image is the original image obtained from the IVUS system. We used a commercial available IVUS system (Clear View Ultra, Boston Scientific, USA). The central frequency of the rotating IVUS probe (Atlantis SR Pro, Boston Scientific, USA) was 40 MHz.

2.1 Moments

Our algorithm uses the moments of an image to compute texture features. The $(p+q)$-th order moment m_{pq} of a function of two variables $f(x,y)$ with respect to the origin (0,0) is defined as[2]:

$$m_{pq} = \int_{-\infty}^{\infty}\int_{-\infty}^{\infty} f(x,y)x^p y^q dxdy \qquad (1)$$

where p,q = 0,1,2, ... Normally the moments are computed over some bounded region. If the function is equal to unity within the region and zero outside the region, the lower order moments (small values of p and q) have well defined interpretations. For example, m_{00} is the area of the region, m_{10} / m_{00} and m_{01} / m_{00} give the x and y coordinates of the centroid for the region, respectively. The m_{20}, m_{11} and m_{02} can be used to derive the amount of elongation o the region, and the orientation of its major axis. The higher order moments give even more detailed shape characteristics of the polygons such as symmetry, etc.

In this paper, as in Tuceryan's work[4], we regard the intensity image as a function of two variables, $f(x,y)$. We compute a fixed number of lower order moments for each pixel in the image (we use $p+q \le 2$). The moments are computed within a small local window around each pixel.

Given a window size W, the coordinates are normalized to the range of [-0.5 , 0.5] and the pixel is located at the center. The moments are computed with respect to this normalized coordinate system. This permits us to compare the set of moments computed for each pixel. We always choose the window width W to be odd so that the pixel (i , j) is centered on a grid point.

Let (i , j) be the pixel coordinates for which the moments are computed. For a pixel with coordinates (k , l) that fall within the window, the normalized coordinates (x_k, y_l) are given by:

$$x_k = \frac{k-i}{W} \qquad y_l = \frac{l-j}{W} \qquad (2)$$

Then the moment $m_{pq}(i,j)$ within a window centered at pixel (i,j) is computed by a discrete sum approximation of Equation (1) that uses the normalized coordinates (x_k, y_l):

$$m_{pq}(i,j) = \sum_{k=-W/2}^{W/2}\sum_{l=-W/2}^{W/2} f(i+k, j+l)x_k^p y_l^q \qquad (3)$$

This discrete computation of the set of moments for a given pixel over a finite rectangular window corresponds to a neighbor operation, and, therefore, it can be interpreted as a convolution of the image with a mask[4].

When we examine the masks, we see that they can be interpreted as local features detectors. For example, the mask for m_{00} corresponds to a box-averaging window, and thus it can be interpreted as computing the total energy within that box. The masks for m_{10} and m_{01} take the form of edge detectors. They would respond to sudden intensity changes in the x and y directions, respectively. The second order moments are not easy to interpret; the only exception being m_{11}, which looks like a cross detector[4].

The set of values for each moment over the entire image can be regarded as a feature image. Let M_k be the k-th such image. If we use n moments, then there will be n such moments images. In our experiments, we used m_{00}, m_{01}, m_{10}, m_{11}, m_{02}, and m_{20}, which result in the images M_1, M_2, M_3, M_4, M_5, and M_6, respectively.

2.2 Radial distance

In this work, we define the radial distance R as the distance from the central pixel of the image to the position of the pixel P under consideration. This distance R is the seventh feature (together with m_{00}, m_{01}, m_{10}, m_{11}, m_{02}, and m_{20}) used in the following clustering of the input image pixels. Based on these features, the pixels were clustered in the clustering block using the Fuzzy C Means algorithm[5].

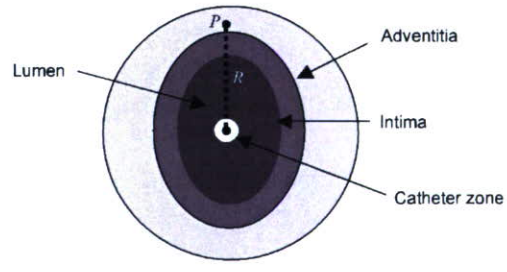

Fig.2 – Illustration of a cross-section of a blood vessel

The number of clusters chosen was four: one cluster for the external region, one for the region between the adventitia and intima, one for the lumen and another one for the catheter zone. After the clustering the image could have its boundaries easily detected by any boundary detection method. However, in order to reduce the irregularities of the borders as well as some small regions around the borders, a

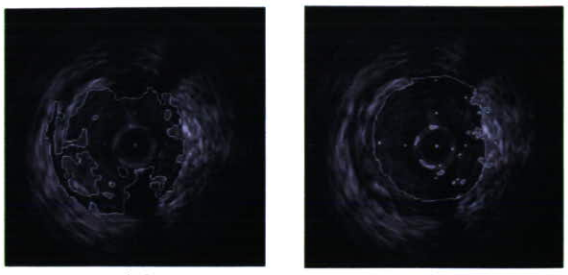

(A) (B)

Fig.3 – Effect of the radial distance feature *R* as one of the components of the feature vector. (A) and (B) are the same images obtained from patient A. (A) Clustered image without using the radial distance feature *R*. (B) Clustered image using the radial distance feature *R*.

morphological filtering was done prior to the boundary detection.

2.3 Morphological contour smoothing

Mathematical morphology is a technique of image processing whose value for each pixel in the output image is based on a comparison of the corresponding pixel in the input image with its neighbors. By choosing the size and shape of the neighborhood, we can define a morphological operation that is sensitive to specific shapes in the input image. The neighborhood size and shape are determined by the size and shape of a second, usually much smaller, image called *structuring element*, which together with the input image is regarded as a set. Thus, basic operations of the set theory like union, subtraction and compliment can be carried out with both images. These basic operations can be used to compose other operations like *opening* and *closing*, for example. Opening generally smoothes the contour of an object, breaks narrow isthmuses, and eliminates thin protrusions. Closing also tends to smooth sections of contour, but, as opposed to opening, it generally fuses narrow breaks and long thin gulfs, eliminates small holes and fills gaps in the contour[6].

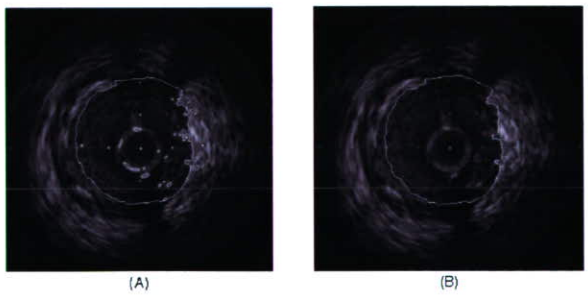

(A) (B)

Fig.4 – (A) Result of the clustering; (B) Result of the morphological contour smoothing

In order to reduce the irregularities of the borders as well as some small regions around the borders, morphological filtering is done prior to boundary detection. This filtering is performed through the application of opening and closing morphological operations with a disk structuring element of size 3. An example of the result of the luminal contour obtained from the clustering process without any contour smoothing can be seen in Fig. 4(A). An example of the luminal contour obtained when the morphological filter is applied after the clustering is shown in Fig.4(B).

3. Analysis of results

Using the system presented above, tests were done with 15 IVUS images of different patients. We can observe in Fig.6 that the boundaries automatically drawn by the proposed system closely resemble the ones drawn manually by an expert medical doctor. In Fig.5 is shown the correlation between the areas of the automatically defined lumen and manually defined lumen. The correlation coefficient was equal to 0.86.

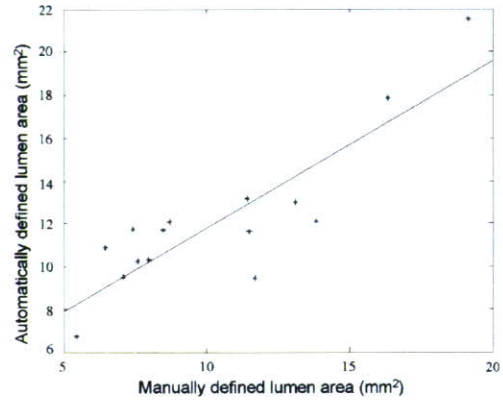

Fig.5 – Correspondence between the lumen area manually defined and the area automatically defined.

The transition between the lumen and the vessel wall as well as the transition between the vessel layers is quite smooth. This makes the boundaries detection based on local features a hard task. However, due to the ability of the local moments in characterization of textured regions, together with the radial distance, it was possible to identify the pixels that belong to the lumen region and those that do not belong. With this method only the lumen boundary detection achieved a reasonable level of accuracy. The outer vessel border was not accurately detected so far, mainly, due to the much more smooth transition from the vessel wall to surrounding tissues. To overcome this difficulty, it seems that more global features should be added to the system as has been studied by Brusseau[2] and Bovenkamp[3].

The effectiveness of the proposed radial distance feature *R* can be observed in Fig.3. In Fig.3(A) we can see an example of segmentation without using the feature *R*. We can see that in this case the resulting segmentation is more irregular and contains some sub-regions segmented inside the lumen region. This over-segmentation occurs mainly because of some texture and gray level changes inside the lumen region. When the radial distance feature is added to the clustering process, the differences among these segmented sub-regions are overcome because they acquire a feature that is similar in most of them, and then this strongly influences the clustering results.

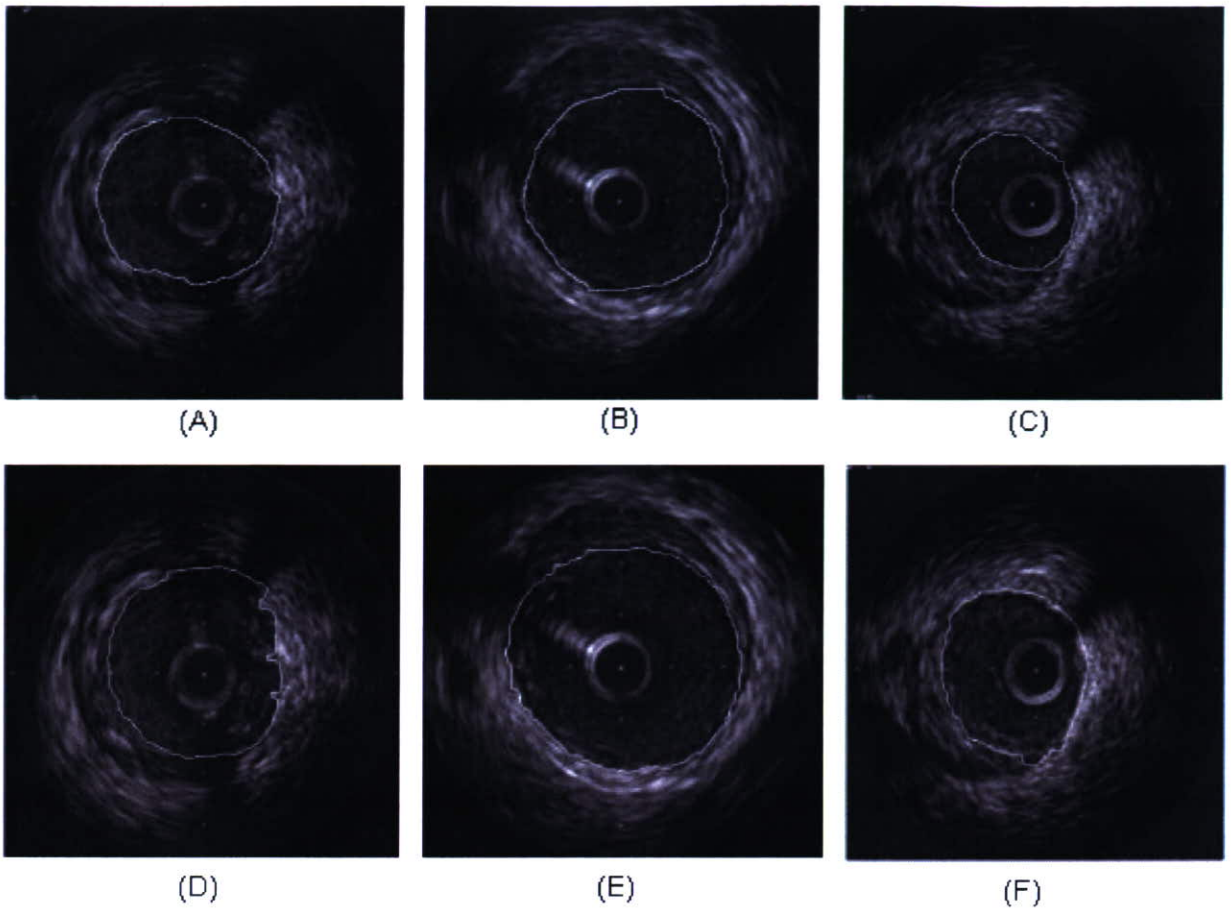

Fig. 6 - Example of luminal contour detection. (A),(B) and (C) are images manually segmented. (D),(E) and (F) are the corresponding images automatically segmented.

Thus, we can obtain a more regular and compact segmentation of the lumen region, as shown in Fig.3(B).

4. Conclusion

Based on our tests, we can conclude that the moment-based texture features together with the radial distance are feasible components for a feature vector in IVUS image segmentation when the aim is to find the luminal contour.

The process was improved when the morphological smoothing filtering was carried out after the clustering and before the boundary detection process. Tests performed with 15 images from different patients resulted in a correlation coefficient of 0.86 between the lumen areas automatically detected and lumen areas manually detected.

Only the segmentation of the luminal contour has been considered. As future work, we plan to extend this method to detection of the vessel contour, which is necessary for assessment of the degree of vessel stenosis. In pratical terms, once having determined the position of the blood-tissue interface, the luminal area will be excluded and the second contour will be searched in the remaining region.

References

[1] X. Zhang, R. Charles and M. Sonka, Tissue characterization in intravascular ultrasound images, IEEE Transaction on Medical Imaging, Vol. 17, No. 6, pp. 889-899, 1998.

[2] E. Brusseau, C.L. Korte, C.L., F. Mastik, J. Schaar and A.F.W. van der Steen, Fully automatic luminal contour segmentation in intracoronary ultrasound imaging - a statistical approach, IEEE Transactions on Medical Imaging, Vol. 23, No. 5, pp.554-566, May 2004

[3] E.G.P. Bovenkamp, J. Dijkstra, J.G. Bosch, and J.H.C. Reiber, Multi-agent segmentation of IVUS images, Pattern Recognition, Elsevier, Vol. 37, pp. 647-663, No. 4, April 2004.

[4] M. Tuceryan, Moment based texture segmentation, Proceedings of 11th IAPR International Conference on Image, Speech ,Signal Analysis and Pattern Recognition, pp.45-48, 1992

[5] J.C. Bezdek, Pattern recognition with fuzzy objective function algorithms, Plenum Press, New York, 1981

[6] R.C. Gonzalez and R. E. Woods, Digital image processing, Prentice Hall, New Jersey, 2002.

Proceedings of the 2005 IEEE
Engineering in Medicine and Biology 27th Annual Conference
Shanghai, China, September 1-4, 2005

Detection of Luminal Contour Using Fuzzy Clustering and Mathematical Morphology in Intravascular Ultrasound Images

Esmeraldo dos Santos Filho, Makoto Yoshizawa, Akira Tanaka, Yoshifumi Saijo and Takahiro Iwamoto

***Abstract*— An innovative application of fuzzy clustering and mathematical morphology for the problem of luminal contour detection in intravascular ultrasound images is presented. Median and standard deviation are used as features for segmentation process. Comparison was made with gold standard segmented images obtained from the average of images segmented by experienced medical doctors. Tests were carried out with 20 *in vivo* coronary images obtained from different patients. High correlation coefficients were found between lumen regions manually and automatically defined when area, mean gray level, and standard deviation of the lumen regions were compared.**

I. INTRODUCTION

Cardiovascular pathologies are one of the main causes of mortality in the Western world. Atherosclerosis is a disease in which the arteries are hardened and narrowed due to the gradual build-up of plaque on their inner wall.

The intravascular ultrasound (IVUS) is a catheter-based technique that generates cross-sectional images of the lumen, plaque and vessel wall. Coronary artery atherosclerosis severity is mainly deduced from the degree of vessel stenosis induced by the atherosclerotic plaque formation. It is generally estimated, from IVUS images, by segmenting and measuring the lumen area, and by referencing it to the total cross-sectional area of the vessel. With the majority of IVUS systems, this work is generally performed manually. However, due to the tedious nature of manual tracing, many research groups have worked on developing automatic segmentation methods for IVUS images.

Brusseau *et al* [1] developed a fully automatic method for luminal contour segmentation in IVUS images based on an active contour that evolves until it optimally separate regions with different statistical properties. Their system used a phase array transducer and achieved high accuracy level. However, no mention was done about the case of the largely used rotating systems.

Bovenkamp *et al* [2] developed an automatic multi-agent based system for luminal contour segmentation. Each agent cooperates with other agents to come to a consistent overall image segmentation. However, the complexity of this system may lead to time delay in case of conflict among the agents.

This work was supported by Health and Labor Sciences Research Grants H15-Fiji-001 of Ministry of Health Labor and Welfare of Japan and the Grant of Tohoku University 21 COE Program: 'Future Medical Engineering based on Bio-nanotechnology'.

Esmerado dos Santos Filho is with Graduate School of Engineering, Tohoku University, Aoba 6-6-05, Aoba-ku, Sendai 980-8579, Japan (esmeraldo@ieee.org)

Makoto Yoshizawa is with Information Synergy Center, Tohoku University, Japan (yoshizawa@ieee.org)

Akira Tanaka is with College of Symbiotic Systems Science, Fukushima University, Japan (a-tanaka@ieee.org)

Yoshifumi Saijo is with Institute of Developement, Aging and Cancer, Tohoku University, Japan (saijo@idac.tohoku.ac.jp)

Takahiro Iwamoto is with Graduate School of Engineering, Tohoku University, Japan (iwamoto@ecei.tohoku.ac.jp)

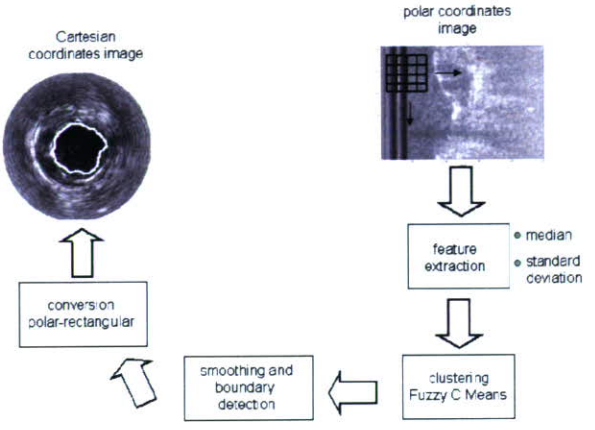

Fig. 1. Block diagram of the proposed algorithm for luminal contour segmentation

In this paper, like those by Brusseau [1] and Bovenkamp [2], we proposed a system for automatic luminal contour segmentation. Unlike the Brusseau's system [1] our system is applied on images obtained from a rotating IVUS system due to the fact that these systems are largely used in clinical settings. Instead of a multi-agent system, as proposed by Bovenkamp [2], we used a fuzzy clustering based in on simple statistics, mean and standard deviation, obtained from a sliding window that scans the entire input image.

II. MATERIALS AND METHODS

In this work, we used a commercial available IVUS system (Clear View Ultra, Boston Scientific, USA). The central frequency of the rotating IVUS probe (Atlantis SR Pro, Boston Scientific, USA) was 40 MHz.

After the acquisition the RF signal was used to generate polar coordinate system images to facilitate the search for the lumen boundary. A block diagram of the proposed system is shown in Fig.1

A. Feature extraction and fuzzy clustering

Using a 7×7 sliding window, the input polar coordinate system image was scanned from the left to the right and from top to bottom. For each position of this window the median and standard deviation of the gray level of the pixels included in the window were calculated and became the features used

to represent the pixel in the center of the window. This process was repeated for every pixel of the input image.

The Fuzzy C-means algorithm [3] was used for clustering of the pixels of the input image on basis of their median and standard deviation features. The number of clusters was defined equal to two: one for lumen region and one for the vessel and external region. The catheter zone was ignored during the clustering process.

One example of the clustering result can be seen in Fig.2. In Fig2(A) we have an example of polar coordinate system input image and in Fig.2(B) is shown the corresponding clustered image.

B. Smoothing and boundary detection

After the clustering a morphological filter was applied to eliminate some irregularities of the image and small segmented regions as well. Thus, the clustered image was first submitted to an operation of region filling followed by closing with disk structuring element of size 5. This filtering helped to obtain a more regular boundary as shown in Fig.2(C).

After the morphological filtering the boundary between lumen and vessel was detected by scanning the filtered image from the left to the right until the transition from black to white be found and then, immediately, jumping to the next line. With this procedure was possible detect the lumen boundary as shown in Fig.2(D). After that the lumen boundary was converted to Cartesian system , as shown in Fig.2(E), and superposed on the original image as shown in Fig.2(F).

C. Evaluation method

In order to evaluate the accuracy of the performed segmentation, the results should be compared with the real lumen shape. Because the actual shape is not known, a gold standard reference image is obtained from manual segmentations.

The manual segmentation results show variability between different observers and sometimes also between the two

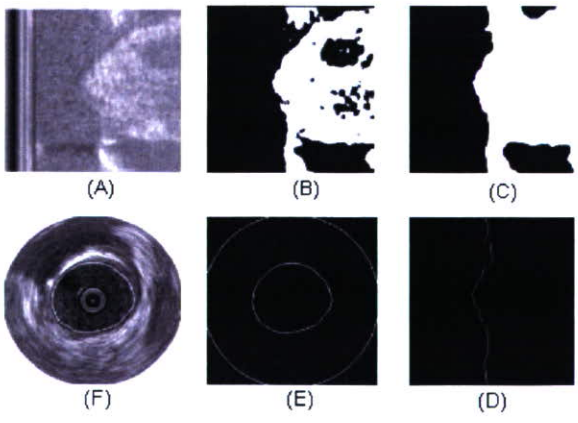

Fig. 2. Example of automatically segmented image. (A) Polar coordinate system input image. (B) Clustered image. (C) morphologically filtered image. (D) Detected lumen boundary. (E) Lumen boundary converted to Cartesian system. (F) Final output image.

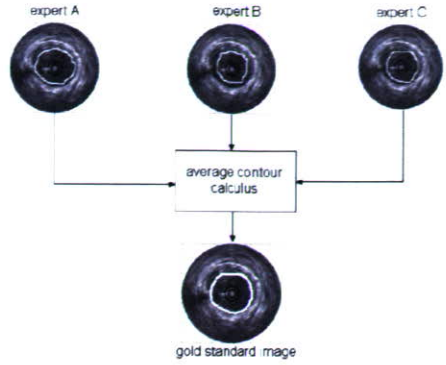

Fig. 3. Block diagram of gold standard generation procedure

traces of one observer, so a single manual segmentation cannot act as a standard. We therefore derive a gold standard reference image by calculating the average shape of the manual segmentations using shape-based interpolation [5]. This technique uses the shapes of the binary object in each manual segmentation to calculate so-called distance scenes. In a distance scene, each pixel is given a value the represents the nearest pixel of the object, i.e., the lumen contour. Pixels inside the lumen are given negative distance values.

The average shape is then calculated by adding the distance scenes of all manual segmentations; the transition from positive to negative values yields the average contour as has been done in Bouma's work [6]. In this work we used images segmented by three experienced medical doctors to generate the gold standard images as illustrated in Fig.3.

In order to obtain a reliable comparison, the automatically segmented images as well as their corresponding gold standard were divided in four quadrants similarly as has been proposed by Allonso's work [7]. An example is shown in Fig.4. For each quadrant the variance, mean gray level, and area were calculated. The correlation between the features extracted from the gold standard and the corresponding features extracted from automatically segmented images are shown in Fig.5,6, and 7.

III. RESULTS AND DISCUSSION

Using the system presented above, tests were done with 20 *in vivo* coronary IVUS images from different patients. Fig.5,6, and 7 show the correlation between features of the automatically defined lumen regions and manually defined lumen region. The correlation coefficient was equal to 0.94

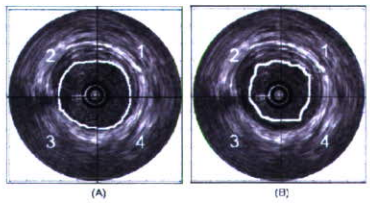

Fig. 4. Example of images divided in quadrants for comparison

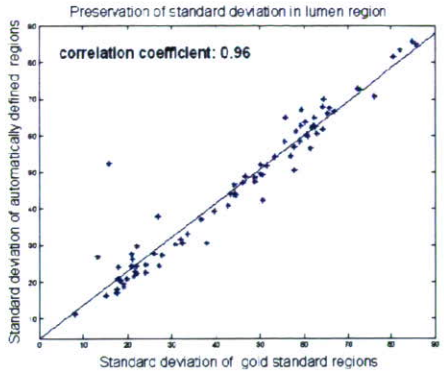

Fig. 5. Correspondence between the standard deviation of the pixels gray level calculated in the lumen region manually defined and the lumen region automatically defined

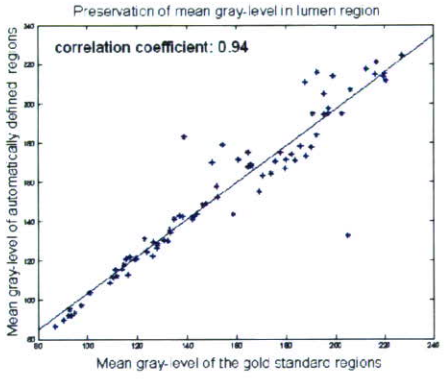

Fig. 6. Correspondence between the mean gray level calculated in the lumen region manually defined and the lumen region automatically defined

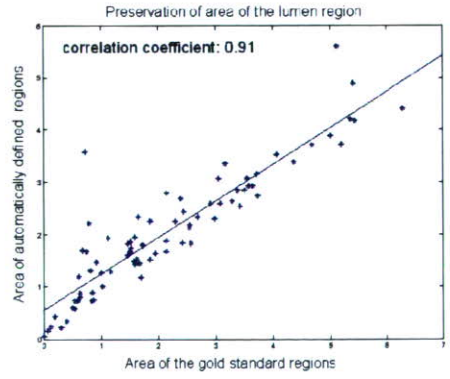

Fig. 7. Correspondence between the lumen area manually defined and the area automatically defined

for the feature mean gray-level, 0.96 for the feature standard deviation, and 0.91 for the feature area.

Some examples of the results are shown in Fig.8 together with the corresponding gold standard images comparison. We can observe that the images segmented automatically by the proposed algorithm closely resemble the gold standard ones.

Some tests were also carried out using images obtained from phantoms due to the fact that in the phantom images the lumen contour is easily detected visually and then may be used for asses the accuracy of the proposed segmentation method. An example que be seen in Fig.9.

The morphological filtering together with the method for search for boundary described in Section II-B were effective in finding the lumen border. This process could be easily performed in the polar coordinate system image but would be not so easy to perform in the Cartesian system image usually used.

The proposed algorithm cannot detect the external vessel contour due to the much more smooth transition between the external vessel wall and the surrounding tissues and the lack of contrast. It seems that more high-level knowledge should be added to the system to make it possible to detect the vessel external contour.

IV. CONCLUSIONS

A system for automatic segmentation of luminal contour was presented. The segmentation was performed through fuzzy clustering using the median and standard deviation of the pixels inside a sliding window as pixel features. After the clustering a morphological filtering was done and the lumen boundary was detected. This method presented high level level of accuracy when compared with gold standard segmented images. However, only the luminal contour was detected. As future work, we plan to extend this method to detection of the vessel contour, which is necessary for assessment of the degree of vessel stenosis. In practical terms, once having determined the position of the blood-tissue interface, the luminal area will be excluded and the second contour will be searched in the remaining region.

REFERENCES

[1] E. Brusseau, C.L. Korte, F. Mastik, J. Schaa and A.F.W. van der Steen, Fully automatic luminal contour segmentation in intracoronary ultrasound imaging - a statistical approach, *IEEE Trans. on Medical Imaging*, vol. 23, 2004, pp.554-566.

[2] E.G.P. Bovenkamp, J. Dijkstra, J.G. Bosch and J.H.C. Reiber, Multi-agent segmentation of IVUS images, *Pattern Recognition*, vol.37, 2004, pp.647-663.

[3] J.C. Bezdek,*Pattern recognition with fuzzy objective function algorithms*,Plenum Press, New York; 1981.

[4] R.C. Gonzales and R.E. Woods, *Digital image processing*,Prentice Hall, New Jersey; 2002.

[5] S.P. Raya and J.K. Udupa, Shape-based interpolation of multidimensional objects, *IEEE Trans. Medical Imaging*, vol.9, 1990, pp.32-42.

[6] C.J. Bouma, W. J. Niessen, K. J. Zuiderveld, E. J. Gussenhoven and A. Viergever, Automated lumen definition from 30 MHz intravascular ultrasound images, *Medical Image Analysis*, vol.1, 1997, pp.363-377.

[7] F. Alonso, M.E. Algorri, F. Flores-Mangas, Composite Index for the quantitative evaluation of image segmentation results, *Proceedings of the 26th Annual International Conference of the IEEE EMBS*, San Francisco, CA, USA, 2004, pp.1794-1797.